The Astrophysical Journal Supplement Series, 195:23 (10pp), 2011 August doi:10.1088/0067-0049/195/2/23

COMPARISON OF MILLIMETER-WAVE AND X-RAY EMISSION IN SEYFERT GALAXIES

R. R. Monje, A. W. Blain, and T. G. Phillips
Division of Physics, Mathematics and Astronomy, California Institute of Technology, Pasadena, CA 91125-4700, USA
Received 2010 January 7; accepted 2011 June 20; published 2011 August 4

ABSTRACT

We compare the emission at multiple wavelengths of an extended Seyfert galaxy sample, including both types of Seyfert nuclei. We use the Caltech Submillimeter Observatory to observe the CO $J = 2$–1 transition line in a sample of 45 Seyfert galaxies and detect 35 of them. The galaxies are selected by their joint soft X-ray (0.1–2.4 keV) and far-infrared ($\lambda = 60$–100 μm) emission from the *ROSAT*/*IRAS* sample. Since the CO line widths ($W_{\rm CO}$) reflect the orbital motion in the gravitational potential of the host galaxy, we study how the kinematics are affected by the central massive black hole (BH), using the X-ray luminosity. A significant correlation is found between the CO line width and hard (0.3–8 keV from *Chandra* and *XMM-Newton*) X-ray luminosity for both types of Seyfert nuclei. Assuming an Eddington accretion to estimate the BH mass ($M_{\rm BH}$) from the X-ray luminosity, the $W_{\rm CO}$–L_X relation establishes a direct connection between the kinematics of the molecular gas of the host galaxy and the nuclear activity, and corroborates the previous studies that show that the CO is a good surrogate for the bulge mass. We also find a tight correlation between the (soft and hard) X-ray and the CO luminosities for both Seyfert types. These results indicate a direct relation between the molecular gas (i.e., star formation activity) of the host galaxy and the nuclear activity. To establish a clear causal connection between molecular gas and the fueling of nuclear activity, high-resolution maps (<100 pc) of the CO emission of our sample will be required and provided in a forthcoming Atacama Large Millimeter Array observation.

Key words: galaxies: active – galaxies: ISM – galaxies: nuclei – galaxies: Seyfert

Online-only material: color figures

1. INTRODUCTION

Seyfert galaxies are classified into two types based solely on their optical spectrum properties. Type 1 Seyferts (Sy1s) are those with very broad H I, He I, and He II emission lines. The forbidden lines [O III], [N II], and [S II], though narrower than the very broad permitted lines, are still broader than the emission lines in most starburst galaxies. Type 2 Seyferts (Sy2s) have permitted and forbidden lines with approximately the same FWHM, similar to the FWHMs of the forbidden lines in Seyfert 1s, but do not present a broad-line feature (Osterbrock & Ferland 2000). Evidence now exists that the main differences in the optical spectra are due to Seyfert nuclei being surrounded by a torus of dusty, obscuring gas a few parsecs from the center. In Sy1s the orientation of the torus axis is close to the line of sight allowing direct observations of the inner broader region associated with the accretion disk of the active galactic nucleus (AGN). In type 2 nuclei, the orientation of the torus shields the nucleus from direct view and only the more extended narrow-line clouds are observed. Several studies analyzing the properties of Seyfert nuclei galaxies have reported a difference in the infrared properties between the Seyfert types, where type 2 nuclei present nearly an order of magnitude enhancement of their infrared emission from their disk with respect to those with type 1 nuclei (Edelson et al. 1987; Maiolino et al. 1995). These results can be easily explained in terms of an elevated rate of star formation of massive stars in galaxies with type 2 nuclei. In addition, Maiolino et al. (1997) found, through their ^{12}CO (1–0) observations of a large sample of Seyfert galaxies, no significant difference in the total amount of molecular gas as a function of the Seyfert nuclear type. Therefore, they concluded that the total amount of molecular gas is not responsible for the enhanced star-forming activity in Seyfert 2 hosts. Contrary to those observations, Heckman et al. (1989) and Curran (2000), using observations of the CO $J = 1$–0 line, found that Sy2s do indeed have a higher molecular gas content than Seyfert 1s. Curran (2000) found that for Seyfert galaxies with far-infrared (FIR) luminosity ($L_{\rm FIR}$) $\approx 10^{10}\,L_{\odot}$, the CO/FIR luminosity ratio in type 2 is at least three times that in type 1 sources. They suggested that this molecular gas may be related in some indirect way to the nuclear material hypothesized to obscure the broad-line region in Sy2s. In this paper, we study the molecular gas content of Seyfert types by comparing the luminosities of a higher excitation line (CO $J = 2$–1) to the FIR and X-ray luminosities of a sample of 35 active galaxies. The sources were selected by their soft X-ray (0.1–2.4 keV) and FIR emission from a *ROSAT*/*IRAS* sample generated originally by Boller et al. (1992) and modified by Condon et al. (1998), who used new Very Large Array images of all the objects to eliminate uncertainties coming from the original *ROSAT* and *IRAS* positions. Molecular gas is important not only to support the star formation activity in the different Seyfert types, but also to understand the powering mechanism of the nuclear activity in AGNs. The source of the accreted gas is still unclear. Most studies suggest that the massive black holes (BHs) are fed by infalling interstellar gas, which is mostly in molecular form in the central kiloparsec of spiral galaxies. Single dish observations of CO emission cannot give a direct answer to the molecular-gas–nuclear-activity relation, since any relation between the fueling (through CO luminosity) and the massive BH data, such as X-ray luminosity (assuming most of the X-ray luminosity in Seyfert galaxies comes from the accretion disk around the massive BH sitting in the center of the galaxy), must be searched for in the central few 100 pc of nearby AGNs. However, Yamada (1994) and Kawakatu et al. (2005) reveal an interesting close relation between $L_{\rm CO}$ and L_X in Seyfert 1s at low and high redshift, respectively. In this paper, we study the properties of an extended Seyfert galaxy sample including both types of Seyfert

Table 1
Summary of Galaxies

Galaxy	Name	Type	Velocity (km s^{-1})	Redshift	i^a (deg)
IRAS 00076–0459	MRK 0937	SBa/b, H II, Sy2	8846	0.029507	29.1
IRAS 00317–2142	ESO 540- G 001	SB(r1)bc, Sy1.8	8048	0.026845	33
IRAS 04260+6444	NGC 1569	IBm;Sbrst, Sy1	−104	−0.000347	64.7
IRAS 04565+0454	UGC 03223	SBa Sy1	4683	0.015621	61.5
IRAS 05128+5308	CGCG 258-006	S, Sy1.8	8482	0.028293	68.6
IRAS 05497–0728	NGC 2110	SAB0-, Sy2	2335	0.007789	46.4
IRAS 06280+6342	UGC 03478	Sb, Sy1.2	3828	0.012769	76.7
IRAS 07388+4955	UGC 03973	SBb, Sy1.2	6652	0.022189	36.7
IRAS 08331–0354	NGC 2617	Sy1.8	4261	0.014213	39.8
IRAS 09585+5555	NGC 3079	SB(s)c;LINER, Sy2	1116	0.00372	82.5
IRAS 10126+7339	NGC 3147	SA(rs)bc;H II, Sy2	2820	0.009407	29.5
IRAS 10291+6517	NGC 3259	SAB(rs)bc:BLAGN, Sy1	1686	0.005624	60.7
IRAS 10295–1831	2MASX J10315733–1846333	Sp, Sy1	12070	0.040261	20.3
IRAS 10589–1210	MCG -02-28-039	Sy1.5	7720	0.025751	59.9
IRAS 11033+7250	NGC 3516	(R)SB(s): Sy1.5	2649	0.008836	37.0
IRAS 11083–2813	ESO 438- G 009	RSB(rl)ab Sy1.5	7199	0.024013	50.8
IRAS 11112+0951	IC 2637	E+, pec, Sy1.5	8763	0.029230	35
IRAS 11210–0823	NGC 3660	SB(r)bc Sy2	3683	0.012285	32.9
IRAS 11376+2458	NGC 3798	SB0, Sy1	3552	0.011848	90
IRAS 11395+1033	NGC 3822	Sb Sy2	6138	0.020474	76.0
IRAS 11500–0455	MCG -01-30-041	(R)SB(rs)ab, Sy1.8	5641	0.018816	55.5
IRAS 12373–1120	MESSIER 104	SA(s)a;LINER, Sy1.9	1024	0.003416	78.5
IRAS 12393+3520	NGC 4619	SB(r)b pec? Sy1	6927	0.023106	14.6
IRAS 12409+7823	2MASX J12423600+7807203	Sy1.9	6625	0.022100	75.7
IRAS 12495–1308	NGC 4748	Sa Sy1	4386	0.014630	53.2
IRAS 13218–1929	2MASX J13243528–1945114	(R'_1)SB(l:)a, Sy1.9	5284	0.017625	...
IRAS 14060+7207	NGC 5643	Sy 1.9	10251	0.034194	54.2
IRAS 14105+3932	NGC 5515	Sab, Sy1.9	7719	0.025749	62.6
IRAS 14156+2522	NGC 5548	(R')SA(s)0/a Sy1.5	5149	0.017175	41.4
IRAS 14294–4357	NGC 5643	SAB(rs)c, Sy2	1199	0.003999	30.5
IRAS 15361–0313	CGCG 022-021	H II, Sy1.9	7137	0.023806	68.7
IRAS 15564+6359	CGCG 319-034	Sy1.9	9023	0.030097	54.2
IRAS 16277+2433	VV 807	Sy1.9	11241	0.037496	57.2
IRAS 17020+4544	B3 1702+457	SBab;Sy1,Sy2	18107	0.060400	59.9
IRAS 17023–0128	UGC 10683	S0+ pec: Sy1.5	9149	0.030518	41.3
IRAS 18001+6638	NGC 6552	SB?, Sy2	7942	0.026492	47.4
IRAS 19399–1026	NGC 6814	SAB(rs)bc;H II, Sy1.5	1563	0.005214	85.6
IRAS 20069+5929	CGCG 303-017	Sbrst, Sy2	11132	0.037132	48.8
IRAS 20437+5929	MRK 0896	SBb, Sy1	7922	0.026424	64.0
IRAS 22062–2803	NGC 7214	SB(s)bc pec: Sy1.2	6934	0.023128	47.3
IRAS 22330–2618	NGC 7314	SAB(rs)bc, Sy1.9	1428	0.004763	70.3
IRAS 22595+1541	NGC 7465	(R')SB(s): Sy2	1968	0.006565	63.4
IRAS 23111+1344	NGC 7525	E, Sy1.5	12262	0.040900	30.6
IRAS 23163–0001	NGC 7603	SA(rs)b: pec, Sy1.5	8851	0.029524	61.5
IRAS 23279–0244	UM 163	SB(r)b pec:;H II, Sy1	10022	0.033430	65.1
IRAS 23566–0424	IC 1490	SA(rs)b pec:, Sy1	5744	0.019160	55.8

Note.
[a] Inclination to the line of sight obtained from the HyperLeda database.

galaxies, from the kinematics and multi-wavelength luminosity comparison point of view. In Section 2, observations and results in terms of line intensities, correlation coefficients, and linear fits are presented. In Section 3, we summarize the results and discuss the interpretation of the CO line width (W_{CO})–L_X, L_{CO}–L_{FIR} and L_{CO}–L_X relations.

2. OBSERVATIONS AND RESULTS

We have used the 10.4 m Caltech Submillimeter Observatory (CSO) telescope to observe the CO $J = 2$–1 transition line toward the center of 45 Seyfert galaxies and have detected 35 of them. Table 1 lists the source parameters obtained from the NASA/IPAC Extragalactic Database[1] and the HyperLeda database.[2] The observations were mostly done during the winter and spring of 2009, with system noise temperatures typically 300–400 K. Pointing was checked regularly on planets with typical pointing errors less than 5″ during one night. The CSO beam size for the ^{12}CO $J = 2$–1 line (with rest frequency[3] equal to 230.538 GHz) is approximately 30″ and the beam efficiency is 0.69. Peak intensities in T_A^* scale are shown in Table 2. T_A^* is

[1] See http://nedwww.ipac.caltech.edu/
[2] See http://leda.univ-lyon1.fr/
[3] See http://physics.nist.gov/cgi-bin/micro/table5/start.pl

Table 2
Observational Parameters and Gaussian Line Fits

Source	Size[a] (kpc)	ΔV[b] (km s^{-1})	$I^{c} = \int T_A^* dV$ (K km s^{-1})	*Intensity*[d] (erg cm^{-2} s^{-1} sr^{-1})	S_{CO}[e] (Jy km s^{-1})	log L_{CO}[f] (K km s^{-1} pc^2)	log L_{FIR}[g] ($L_\odot$)	log L_x[h] (erg s^{-1})	S_X[i] (erg s^{-1} cm^{-2})
IRAS 00076–0459	16.71	100 ± 20	1.18 ± 0.2	$2.15 \times 10^{-8} \pm 3.6 \times 10^{-9}$	73.1 ± 12	8.77 ± 0.0059	10.18	42.94	...
IRAS 00317–2142	15.20	150 ± 15	5.45 ± 0.9	$9.93 \times 10^{-8} \pm 1.6 \times 10^{-8}$	335.01 ± 54	9.35 ± 0.0068	10.94	42.81	7.49×10^{-13}
IRAS 04260+6444	0.19	50 ± 7	1.01 ± 0.18	$1.85 \times 10^{-8} \pm 3.3 \times 10^{-9}$	57.69 ± 10	4.8 ± 0.075	...	37.92	1.62×10^{-13}
IRAS 04565+0454	8.85	400 ± 50	1.68 ± 0.2	$3.06 \times 10^{-8} \pm 3.6 \times 10^{-9}$	99.82 ± 12	8.35 ± 0.013	10.06	42.06	...
IRAS 05128+5308	16.02	560 ± 60	4.09 ± 0.7	$7.46 \times 10^{-8} \pm 1.3 \times 10^{-8}$	252.84 ± 44	9.28 ± 0.0067	10.81	42.06	...
IRAS 05497–0728	4.41	...	⩽1.08	...	...	⩽7.55	9.72	40.99	1.04×10^{-11}
IRAS 06280+6342	7.23	270 ± 50	1.79 ± 0.17	$3.26 \times 10^{-8} \pm 3.1 \times 10^{-9}$	105.46 ± 10	8.21 ± 0.013	9.84	42.61	...
IRAS 07388+4955	12.56	450 ± 25	1.21 ± 0.16	$2.19 \times 10^{-8} \pm 2.9 \times 10^{-9}$	73.06 ± 9.7	8.52 ± 0.0079	10.31	43.84	3.18×10^{-11}
IRAS 08331–0354	8.05	180 ± 30	2.22 ± 0.65	$4.04 \times 10^{-8} \pm 1.2 \times 10^{-8}$	131.4 ± 39	8.39 ± 0.036	9.73	42.27	...
IRAS 09585+5555	2.11	400 ± 120	3.21 ± 0.3	$5.84 \times 10^{-8} \pm 5.4 \times 10^{-9}$	184.15 ± 17	7.37 ± 0.034	10.36	40.18	6.39×10^{-13}
IRAS 10126+7339	5.33	430 ± 30	9.33 ± 1.1	$1.70 \times 10^{-7} \pm 2.0 \times 10^{-8}$	544.49 ± 64	8.65 ± 0.024	10.51	41.83	1.05×10^{-12}
IRAS 10291+6517	3.18	500 ± 40	4.28 ± 0.8	$7.81 \times 10^{-8} \pm 1.5 \times 10^{-8}$	247.45 ± 48	7.86 ± 0.083	9.07	40.04	3.31×10^{-14}
IRAS 10295–1831	22.80	150 ± 12	1.45 ± 0.15	$2.64 \times 10^{-8} \pm 2.7 \times 10^{-9}$	92.88 ± 9.5	9.08 ± 0.002	11.02	43.14	...
IRAS 10589–1210	14.58	510 ± 30	1.86 ± 0.2	$3.40 \times 10^{-8} \pm 3.6 \times 10^{-9}$	114.40 ± 12	8.85 ± 0.0048	10.55	41.93	...
IRAS 11033+7250	5.00	...	⩽1.53	...	...	⩽7.81	9.55	41.73	6.21×10^{-11}
IRAS 11083–2813	13.59	300 ± 50	1.95 ± 0.3	$3.56 \times 10^{-8} \pm 5.5 \times 10^{-9}$	119.13 ± 18	8.81 ± 0.0078	10.66	42.95	...
IRAS 11112+0951	16.55	700 ± 50	6.34 ± 0.9	$1.15 \times 10^{-7} \pm 1.6 \times 10^{-8}$	391.90 ± 54	9.49 ± 0.005	10.65	42.91	...
IRAS 11210–0823	6.96	450 ± 30	2.57 ± 0.28	$4.68 \times 10^{-7} \pm 5.1 \times 10^{-9}$	151.25 ± 65	8.33 ± 0.063	9.92	41.61	7.60×10^{-12}
IRAS 11376+2458	6.71	400 ± 50	1.63 ± 0.3	$2.97 \times 10^{-8} \pm 5.5 \times 10^{-9}$	95.84 ± 18	8.09 ± 0.029	9.64	41.46	...
IRAS 11395+1033	11.59	700 ± 200	6.24 ± 0.6	$1.14 \times 10^{-7} \pm 1.1 \times 10^{-8}$	376.55 ± 36	9.17 ± 0.0065	10.58	41.91	...
IRAS 11500–0455	10.65	400 ± 50	1.16 ± 0.16	$2.12 \times 10^{-8} \pm 2.9 \times 10^{-9}$	69.82 ± 9.6	8.36 ± 0.011	10.09	42.12	...
IRAS 12373–1120	1.93	420 ± 50	0.88 ± 0.2	$1.61 \times 10^{-8} \pm 2.2 \times 10^{-9}$	50.89 ± 5.0	6.73 ± 0.042	9.35	40.75	1.61×10^{-12}
IRAS 12393+3520	13.08	210 ± 50	2.52 ± 0.23	$4.60 \times 10^{-8} \pm 4.2 \times 10^{-9}$	153.57 ± 14	8.88 ± 0.005	10.09	42.12	...
IRAS 12409+7823	12.51	...	⩽0.86	...	...	⩽8.38	9.94	41.87	...
IRAS 12495–1308	8.28	300 ± 150	3.24 ± 0.4	$5.91 \times 10^{-8} \pm 7.3 \times 10^{-9}$	192.42 ± 24	8.58 ± 0.014	9.83	42.06	...
IRAS 13218–1929	9.98	360 ± 30	5.01 ± 0.49	$9.11 \times 10^{-8} \pm 8.9 \times 10^{-9}$	299.28 ± 29	8.93 ± 0.0084	10.29	42.14	...
IRAS 14060+7207	19.36	...	⩽1.33	...	...	⩽8.96	10.26	42.15	...
IRAS 14105+3932	14.58	650 ± 50	4.83 ± 0.66	$8.81 \times 10^{-8} \pm 1.2 \times 10^{-8}$	296.26 ± 40	9.26 ± 0.0062	10.63	41.65	...
IRAS 14156+2522	9.73	400 ± 100	2.72 ± 0.66	$4.96 \times 10^{-8} \pm 1.2 \times 10^{-8}$	162.68 ± 39	8.65 ± 0.0022	9.93	43.67	5.39×10^{-11}
IRAS 14294–4357	2.26	180 ± 15	15.88 ± 1.04	$2.89 \times 10^{-7} \pm 1.9 \times 10^{-8}$	911.72 ± 60	8.13 ± 0.024	9.85	40.61	5.31×10^{-13}
IRAS 15361–0313	13.48	400 ± 50	6.40 ± 1.17	$1.17 \times 10^{-7} \pm 2.1 \times 10^{-8}$	389.84 ± 70	9.31 ± 0.0094	10.79	42.02	...
IRAS 15564+6359	17.04	600 ± 60	2.90 ± 0.67	$5.29 \times 10^{-7} \pm 1.2 \times 10^{-8}$	180.10 ± 41	9.18 ± 0.0078	10.41	42.46	1.12×10^{-12}
IRAS 16277+2433	21.23	...	⩽1.45	...	...	⩽9.08	10.53	42.02	2.25×10^{-12}
IRAS 17020+4544	34.20	...	⩽1.11	...	...	⩽9.40	11.02	44.06	1.30×10^{-11}
IRAS 17023–0128	17.28	...	⩽0.76	...	...	⩽8.62	10.42	42.95	...
IRAS 18001+6638	15.00	500 ± 100	1.72 ± 0.5	$3.14 \times 10^{-8} \pm 9.1 \times 10^{-9}$	105.99 ± 31	8.84 ± 0.013	10.63	...	2.94×10^{-13}
IRAS 19399–1026	2.95	140 ± 20	4.36 ± 0.68	$7.95 \times 10^{-8} \pm 1.2 \times 10^{-8}$	251.69 ± 38	7.80 ± 0.048	9.81	41.91	3.08×10^{-11}
IRAS 20437–0259	14.96	...	⩽0.97	...	...	⩽8.61	10.04	43.31	1.06×10^{-11}
IRAS 22062–2803	13.09	500 ± 100	6.97 ± 0.7	$1.27 \times 10^{-7} \pm 1.3 \times 10^{-8}$	423.65 ± 43	9.33 ± 0.0056	10.56	43.04	...
IRAS 22330–2618	2.69	140 ± 50	1.91 ± 0.3	$3.47 \times 10^{-8} \pm 5.5 \times 10^{-9}$	109.76 ± 17	7.37 ± 0.052	9.56	41.17	1.40×10^{-11}
IRAS 22595+1541	3.72	190 ± 30	3.07 ± 0.6	$5.59 \times 10^{-8} \pm 1.1 \times 10^{-8}$	177.79 ± 35	7.85 ± 0.055	9.86	40.54	1.54×10^{-12}
IRAS 23111+1344	23.16	...	⩽0.65	...	...	⩽8.83	10.62	42.81	...
IRAS 23163–0001	16.71	550 ± 100	3.22 ± 0.4	$5.86 \times 10^{-8} \pm 7.3 \times 10^{-9}$	199.27 ± 25	9.21 ± 0.0045	10.41	43.3	3.65×10^{-11}
IRAS 23279–0244	18.93	610 ± 50	4.75 ± 0.6	$8.64 \times 10^{-8} \pm 1.1 \times 10^{-8}$	297.36 ± 38	9.49 ± 0.0036	10.35	42.64	...
IRAS 23566–0424	10.85	470 ± 50	3.35 ± 0.6	$6.09 \times 10^{-8} \pm 1.1 \times 10^{-8}$	201.05 ± 36	8.83 ± 0.014	10.01	42.83	...

Notes.
[a] Beam size at each source.
[b] Width of the line at 20% of the peak intensity.
[c] Integrated intensity in T_A^* corrected for beam efficiency. For the non-detection an upper limit of 3σ has been used.
[d] Intensity from the Rayleigh–Jeans relations.
[e] Flux.
[f] CO luminosity, see the Appendix for derivation.
[g] FIR luminosity in the wavelength range $40\,\mu\text{m} \leqslant \lambda \leqslant 120\,\mu\text{m}$.
[h] Soft (0.1–2.4 keV) X-ray luminosity from *ROSAT* data.
[i] Hard absorption-corrected X-ray flux (0.3–8 keV) from *Chandra* and *XMM-Newton* data.

converted to the main beam brightness scale, T_{mb}, by dividing the T_A^* by the beam efficiency. We have applied the necessary corrections, cold spillover and beam coupling, to those sources with size similar to or smaller than the beam. This gives T_A^*/β, where β is the spillover and beam coupling coefficient. Source sizes have been determined by their optical extent. Since most of our sources are bigger than the beam, we assume extended sources, i.e., $\theta_{beam} \leqslant \theta_{source}$. Therefore, no beam dilution correction has been applied in our temperature calculations. We used a 1 GHz bandwidth FFTS back end with 8192 channels and a 1 GHz bandwidth acousto-optical spectrometer with 2048 channels.

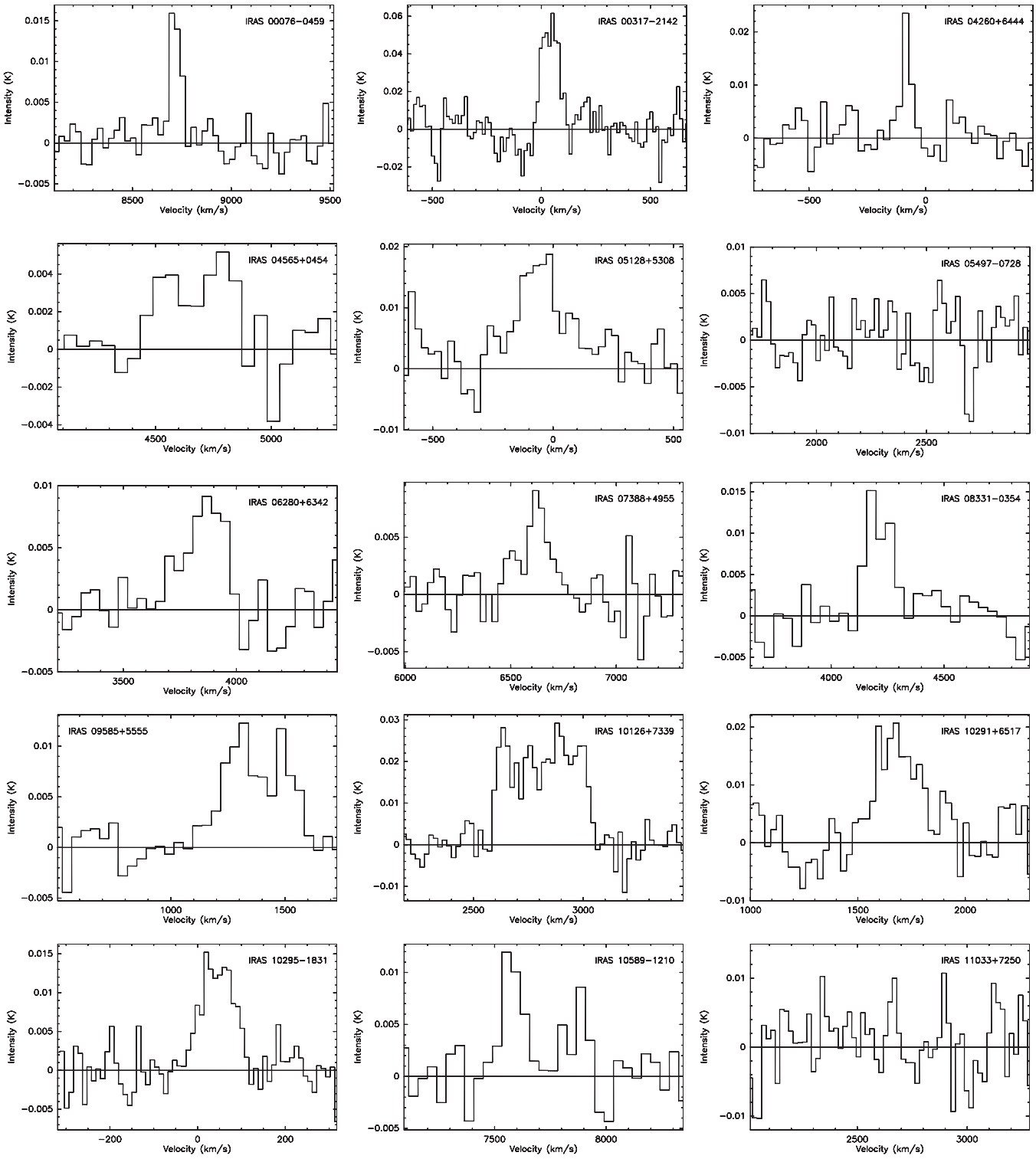

Figure 1. CO $J = 2$–1 observations of our sample. The intensity scale is T_A^* in K.

The molecular line emissions observed for our sample are shown in Figure 1. A first-order polynomial is used to correct the baseline. A 3σ detection has been assumed to calculate the upper limit for the non-detected sources.

2.1. CO Line Width and the Galaxy Inclination

Figure 2 shows that the CO line widths correlate with the galaxy inclination. This result shows that the sources have been correctly identified by Condon et al. (1998) in spite of the large pointing errors of *IRAS* and *ROSAT*. The line widths were measured at 20% of the peak intensity since it gives a more robust measurement of the maximum rotation velocity of the disk as shown by Ho (2007). The galactic disk inclination angles of these Seyfert galaxies were estimated from the HyperLeda database. The CO line width has been also corrected by the blue luminosity ($W_{\rm CO}/L^{1/4}$) to avoid selection effects, since brighter sources rotate faster on average (Tully & Fisher 1977, who

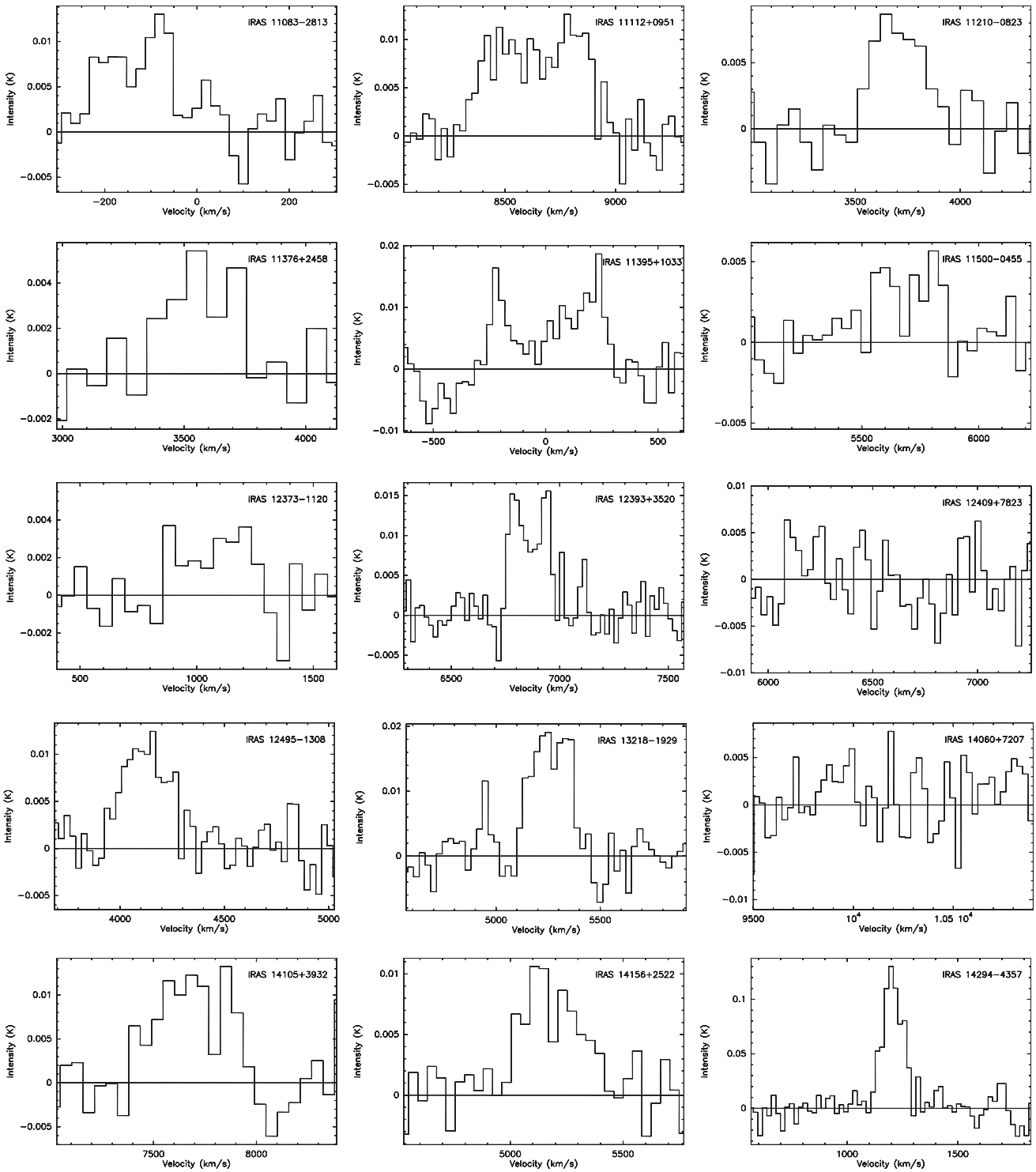

Figure 1. (Continued)

establish that the luminosity, L, is proportional to the fourth power of the rotational velocity, V, i.e., $L \approx V^4$). We notice that when applying the luminosity correction the correlation improves slightly and reduces the spread.

Figure 2 shows that face-on galaxies with smaller inclinations tend to have narrower velocities than edge-on galaxies with larger inclinations, following $\Delta V_{\rm CO} \approx 2V_{\rm MAX} \times \sin(i)$. This is an unsurprising result since the CSO beam samples CO emission on scales of few kiloparsecs (see Table 2). As molecular disks are roughly coplanar with stellar disks on these scales, a rough correlation is expected.

The inclination-corrected CO line-width–redshift correlation has been checked for selection effects of more distant objects being more luminous. In our sample the inclination-corrected CO line-width values are distributed around an average value of 500 km s^{-1} for any redshift, which corresponds to a typical rotational velocity value for spiral galaxies.

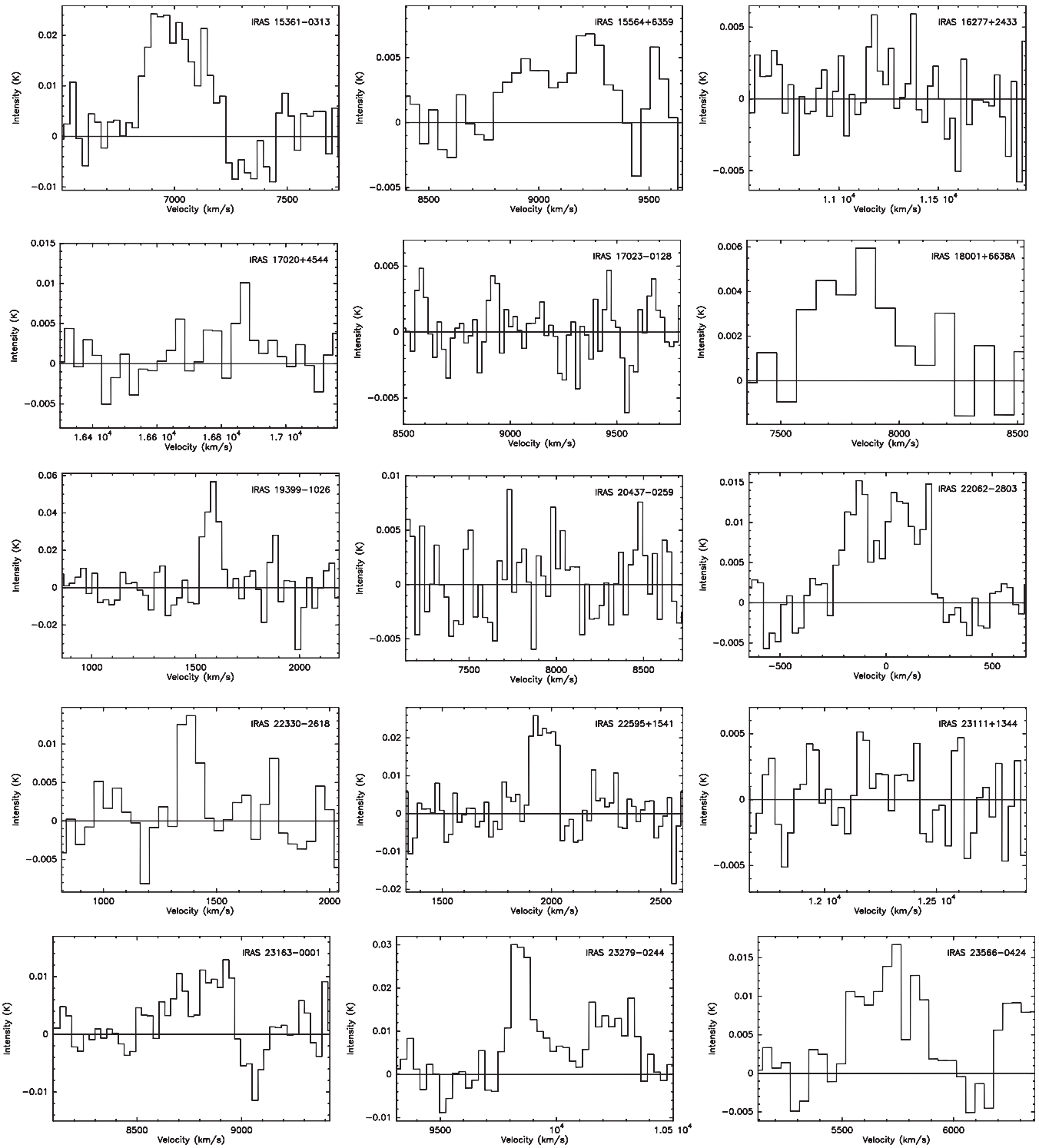

Figure 1. (Continued)

2.2. CO Line Width and the X-Ray Luminosity

We run a simple statistical approach in our investigation of the CO kinematics. For all the Seyfert galaxies with detected CO emission, we examine the possible correlation between the inclination-corrected CO line width and the soft (*ROSAT*, 0.1–2.4 keV) and hard (*Chandra* or *XMM-Newton*, 0.3–8 keV) X-ray luminosity: the data are listed in Table 2. The hard X-ray luminosities in Table 2 are corrected for absorption using the X-ray fitting software from HEASARC.[4] For those type 1 (unobscured) AGNs with no available hard X-ray data, we extrapolate the *ROSAT* (0.5–2 keV) into the *Chandra* (0.3–8 keV) X-ray fluxes, by using the tool PIMMS,[5] applying the net count rate, a power-law spectrum with index $\Gamma = 1.6$, and an estimate of the Galactic neutral hydrogen column density

[4] See http://heasarc.gsfc.nasa.gov
[5] See http://heasarc.gsfc.nasa.gov/Tools/w3pimms.html

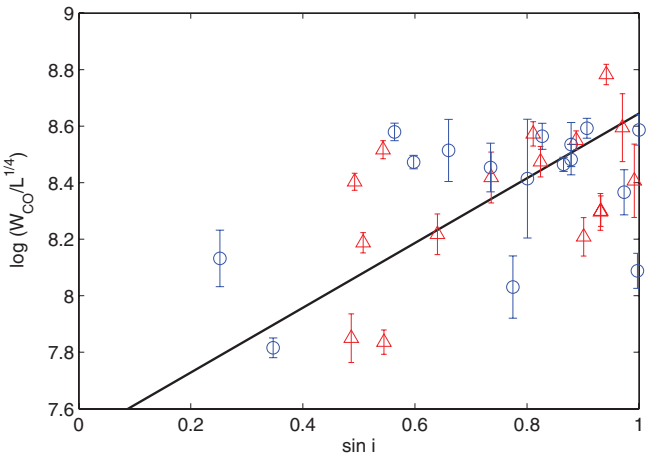

Figure 2. CO line width (km s^{-1}) blue luminosity corrected vs. the sine of the galaxy inclination for the observed sample, Sy1s (circles) and Sy2s (triangles). The CO line width and sin i are correlated with a 0.49 factor and a 0.21 of null probability (see Table 3). The straight line represents the least-squares fit applied to the whole sample (both Sy1s and Sy2s).

(A color version of this figure is available in the online journal.)

from Kalberla et al. (2005). The correlation between X-ray power and CO kinematics has not been examined before, to the best of the authors' knowledge. Figure 3 shows the soft (0.1–2.4 keV; left) and hard (0.3–8 keV; right) X-ray luminosity, L_X, versus the corrected CO line width, $W_{\rm CO}$, in a log–log plot. For the least-squares fit and slope calculations the bisector of the ordinary least-squares regression described in Isobe et al. (1990) has been used. Table 3 lists the results of the L_X–$W_{\rm CO}$ correlation together with the χ^2 value and probabilities. The results from Figure 3 show a significant correlation between the CO line width and both soft and hard X-ray luminosity for Sy1 galaxies, with a correlation coefficient of 0.67 and 0.62 and a null probability of 0.12 and 0.32, respectively. In most Sy2s, the observed 0.1–2.4 keV flux is a mixture of emission from the host galaxy, reflected X-ray emission from the AGNs, and, if the absorbing column density is low enough, some transmitted intrinsic flux. The soft X-ray photons, originating within a radius close to the nucleus ($\leqslant$1 pc), are absorbed by the dusty torus and only the fraction that is scattered toward our line of sight escapes from above and/or below the torus and can be detected, leading to the reduction in observed X-ray flux from Seyfert 2s. Consequently, the soft X-ray luminosity is fainter and does not present a significant correlation with the CO line width.

The observed CO line width reflects the dynamics of the molecular gas in the inner parts of the galaxy. Therefore, we use the CO line widths to estimate the galaxy dynamical masses in this region. For a rotating disk of radius R, the dynamical mass enclosed within R can be determined by the following equation (Solomon et al. 1997):

$$M_{\rm dyn} \approx \frac{R \times \Delta V^2}{2 \times \sin^2(i) \times G}. \quad (1)$$

Here, we assume that the gas emission comes from a rotating disk of outer radius R (in units of kiloparsecs) observed at an inclination angle i. We use a radius, R, equal to the telescope beam FWHM at each source; see Table 2.

At the same time, X-ray luminosity in Seyfert galaxies is related to the black hole mass (BHM; Graham et al. 2001). Given the bolometric luminosity for an AGN, we can estimate the minimum mass of the BH by using the *Eddington limit* relation. In some cases the true bolometric luminosity cannot be calculated easily, as in the case of Seyfert 2s where the optical and ultraviolet (UV) radiation is highly obscured by the dusty torus. However, we can estimate the BHM from the X-ray luminosity: first, by assuming that an important fraction of the bolometric luminosity is emitted in the X-ray range by the central source; second, the AGN luminosity, L, can be estimated from the luminosity in any given band b, L_b, by applying a suitable bolometric correction $f_{{\rm bol},b} = L/L_b$. We will use the bolometric corrections calculated by Marconi et al. (2004).

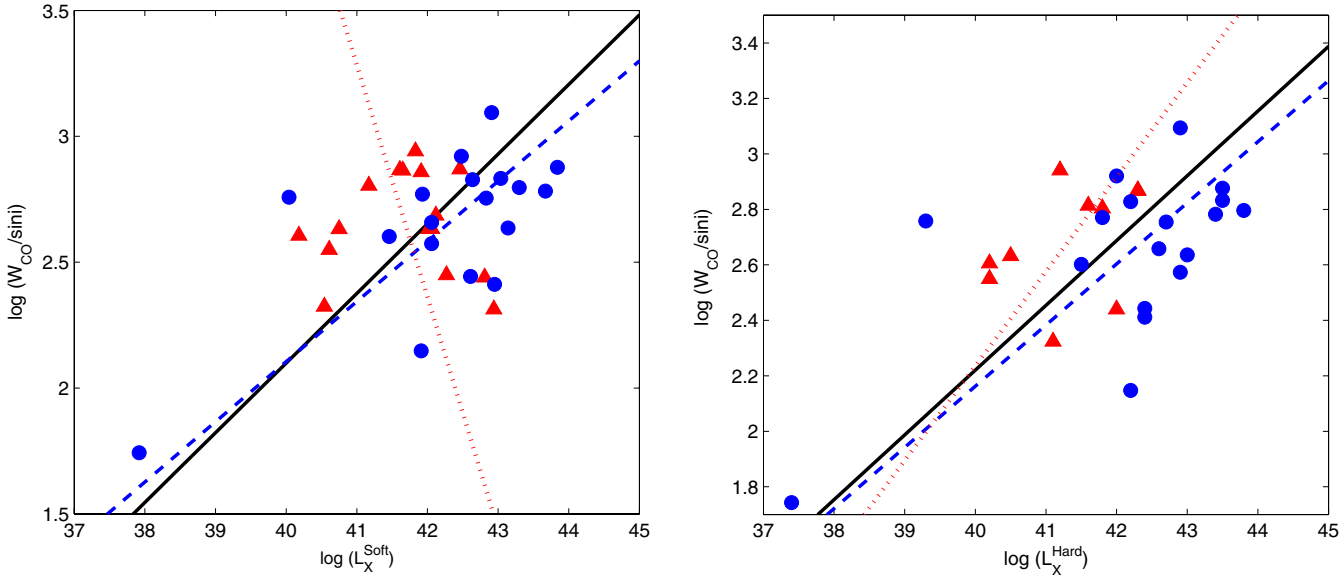

Figure 3. Left: CO line width corrected for inclination (km s^{-1}) vs. soft (0.1–2.4 keV) X-ray luminosity (erg s^{-1}) for the detected Sy1s (circles) and Sy2s (triangles). Right: CO line width corrected for inclination (km s^{-1}) vs. hard (0.3–8 keV) X-ray luminosity (erg s^{-1}) for the detected Sy1s (circles) and Sy2s (triangles). Least-squares fits to the data are indicated by the blue dashed (Sy1s), red dotted (Sy2s), and solid (both Sy1s and Sy2s) lines. The correlation factor for each group and null probability are shown in Table 3.

(A color version of this figure is available in the online journal.)

Table 3
Correlations

Relation	χ^2	Probability (%)	r[a]	Null Probability[b] (%)
$W_{CO}/L^{1/4}$ vs. sin(i)	22.75	82.55	0.49	0.21
log(W_{CO}/sin(i)) vs. log(L_X^{Soft})				
(1) Sy1s	8.80	92.05	0.67	0.12
(2) Sy2s	13.99	45.00	0.02	46.88
(3) Sy1s & Sy2s	24.77	81.50	0.47	0.23
log(W_{CO}/sin(i)) vs. log(L_X^{Hard})				
(1) Sy1s	9.90	87.17	0.62	0.32
(2) Sy2s	6.65	57.48	0.41	11.92
(3) Sy1s & Sy2s	18.62	85.22	0.53	0.18
log(L_{CO}) vs. log(L_X^{Soft})				
(1) Sy1s	4.27	99.84	0.86	2.9×10^{-4}
(2) Sy2s	7.39	94.59	0.71	0.066
(3) Sy1s & Sy2s	12.55	99.95	0.79	1.0×10^{-6}
log(L_{CO}) vs. log(L_X^{Hard})				
(1) Sy1s	4.64	99.73	0.84	5.7×10^{-4}
(2) Sy2s	5.70	76.94	0.60	2.40
(3) Sy1s & Sy2s	10.19	99.84	0.79	1.83×10^{-5}
log(M_{dyn}) vs. log(M_{BH})[c]				
(1) Sy1s	7.60	95.86	0.72	3.54×10^{-2}
(2) Sy2s	3.20	92.05	0.77	0.40
(3) Sy1s & Sy2s	13.19	98.22	0.70	1.58×10^{-2}
log(L_{FIR}) vs. log(L_{CO})				
(1) Sy1s	9.58	84.49	0.60	0.54
(2) Sy2s	5.82	98.99	0.79	3.7×10^{-3}
(3) Sy1s & Sy2s	15.99	99.44	0.71	6.08×10^{-5}

Notes.
[a] The linear correlation coefficient: $r \equiv \frac{N\sum x_i y_i - \sum x_i \sum y_i}{[N\sum x_i^2 - (\sum x_i)^2]^{1/2}[N\sum y_i^2 - (\sum y_i)^2]^{1/2}}$, where r ranges from 0, when there is no correlation to 1, and when there is complete correlation.
[b] Null probability of the correlation (in percentage); indicates the probability that the observed data could have come from an uncorrelated parent population. A small value of the probability implies that the observed variables are probably correlated.
[c] Dynamical mass calculated assuming a rotating disk R, equal to the telescope beam FWHM at each source.

Marconi et al. (2004) use in their calculations the intrinsic luminosity which is the total luminosity directly produced by the accretion process, i.e., the sum of the optical–UV and X-ray luminosities radiated by the accretion disc and hot corona, respectively. We also assume that the X-ray bolometric correction is the same in Sy1 and Sy2 galaxies. As expected from Figure 3, the dynamical and back hole masses present a significant correlation as shown in Figure 4.

2.3. Relation between the CO Luminosity with FIR and X-Ray Luminosities

Figure 5 shows the strong correlation between the FIR luminosity,[6] L_{FIR}, and the CO line luminosity, L_{CO}, of the Seyfert 1s (circles) and Seyfert 2s (triangles) from our sample, in a log–log plot, to confirm the relation observed between far-infrared and CO line luminosity (Rickard & Harvey 1984; Young et al. 1986; Heckman et al. 1989; Sanders et al. 1991; Rigopoulou et al. 1996). The strong correlation is interpreted as the result of the link between the amount of molecular gas and the rate of star formation. The FIR emission for both types of galaxies is very similar with a mean ratio of $L_{FIR}(Sy1)/L_{FIR}(Sy2) \approx 0.88$. This result suggests two different possibilities: first, that the FIR emission comes from dust re-radiation of starlight from regions outside the torus, where both classes of Seyferts have similar properties; and second, the FIR in Seyfert galaxies can be powered by the AGN, i.e., non-thermal radiation coming from the nucleus torus, but in that case, the torus should have a similar covering fraction and optical depth to obtain the same emission from Seyfert 2s as in 1s.

[6] The FIR luminosity, in the wavelength range $40\,\mu m < \lambda < 120\,\mu m$ in (W m^{-2}), is estimated using the relation (Helou et al. 1988) $L_{FIR} = 1.26 \times 10^{-14}(2.58 \times S_{60\,\mu m} + S_{100\,\mu m})$.

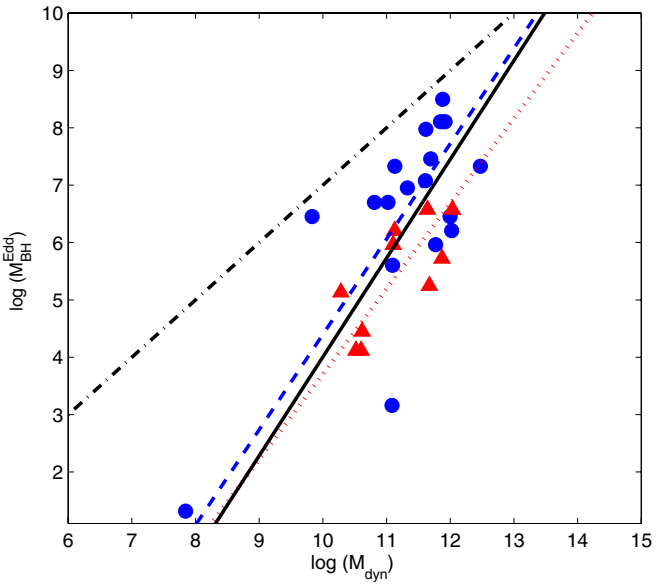

Figure 4. Black hole mass M_{BH}^{Edd} [$M_\odot$] vs. the dynamical mass of the galaxy M_{dyn} [$M_\odot$] for both type 1 (filled circles) and type 2 (triangles) Seyfert galaxies. Least-squares fits to the data are indicated by the blue dashed (Sy1s), red dotted (Sy2s), and solid (both Sy1s and Sy2s) lines. The correlation factor for each group and null probability are shown in Table 3. The M_{BH}–M_{bulge} relation for normal galaxies, i.e., $\langle M_{BH}/M_{bulge}\rangle \sim 0.001$, is indicated by the dot-dashed line.
(A color version of this figure is available in the online journal.)

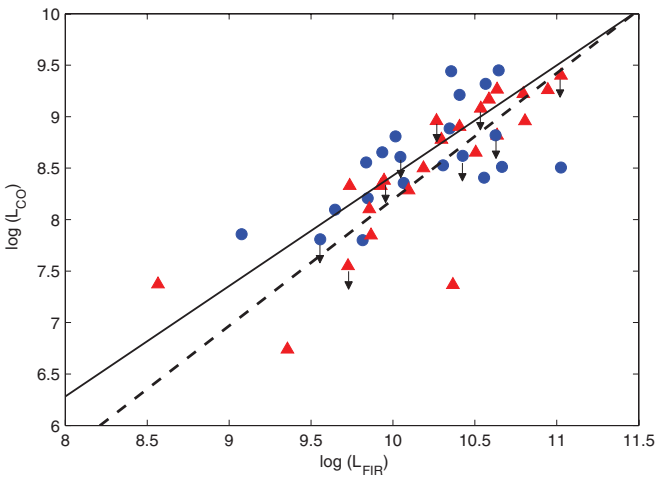

Figure 5. log L_{CO} (K km s^{-1} pc^2) vs. log L_{FIR} [$L_\odot$] for the observed Sy1s (circles) and Sy2s (triangles). Least-squares fits to the data are indicated by the solid (Sy1s) and dashed (Sy2s) lines. The upper limits of the non-detection are plotted as well. The correlation factor for each group and probability of not being correlated are shown in Table 3.
(A color version of this figure is available in the online journal.)

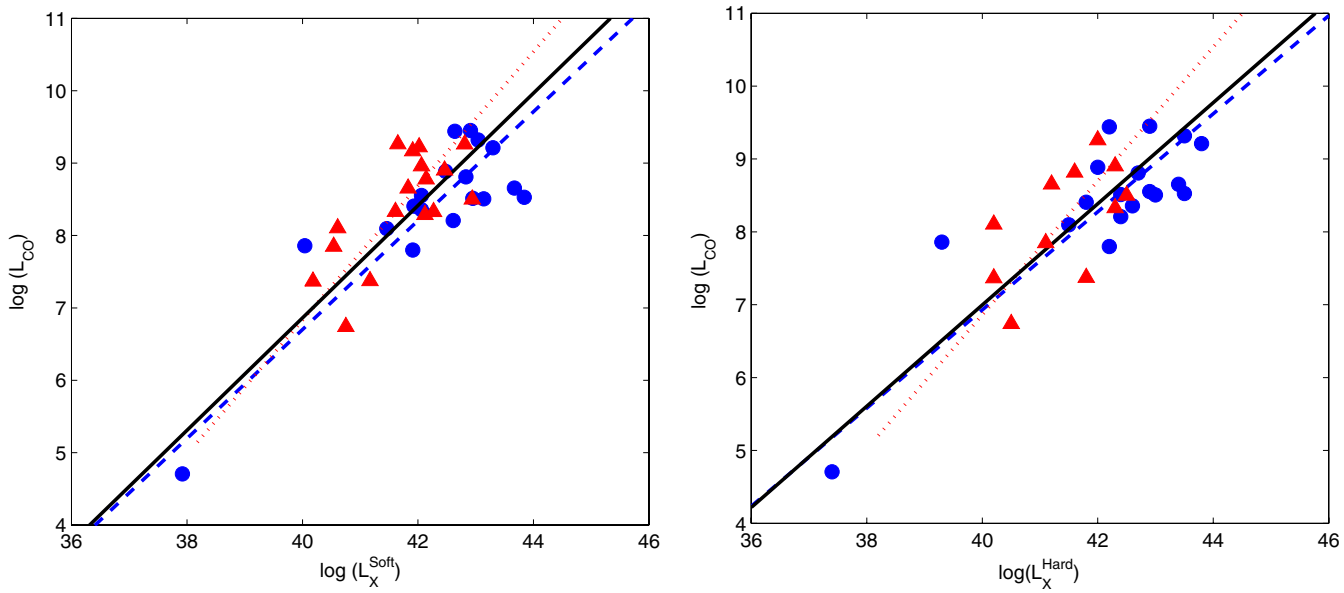

Figure 6. Left: CO luminosity (K km s^{-1} pc^2) vs. soft (0.1–2.4 keV) X-ray luminosity (erg s^{-1}) for the observed Sy1s (circles) and Sy2s (triangles). Right: CO luminosity (K km s^{-1} pc^2) vs. hard (0.3–8 keV) X-ray luminosity (erg s^{-1}). Least-squares fits to the data are indicated by the blue dashed (Sy1s), red dotted (Sy2s), and solid (both Sy1s and Sy2s) lines. The correlation factor for each group and null probability are shown in Table 3.

(A color version of this figure is available in the online journal.)

Studying the relation between the CO and FIR luminosities can give us a better understanding of the origin of FIR emission in Seyfert galaxies, and the relationship between the AGN activity, the star formation, and the interstellar medium via the molecular gas content. Taking the average value of $L_{\rm CO}/L_{\rm FIR}$ for both Seyfert types we obtain the following result:

$$\frac{L_{\rm CO}}{L_{\rm FIR}}({\rm Sy1}) \approx 1.33 \pm 0.13 \times \frac{L_{\rm CO}}{L_{\rm FIR}}({\rm Sy2}) \approx 3.21 \times 10^{-8}\,{\rm K\,km\,s^{-1}\,kpc^2}\,L_{\odot}^{-1}. \quad (2)$$

There is not a significant difference in the total molecular gas content between the two Seyfert types. This result is consistent with the one obtained by Maiolino et al. (1997) establishing that the total amount of molecular gas is not responsible for the enhanced star formation activity observed in Seyfert 2 hosts (Gonzalez-Delgado & Perez 1993).

Another interesting observational result from this survey is the strong correlation between the X-ray and the CO luminosity (see Figure 6) with a null probability of 1.83×10^{-5} and a correlation coefficient of 0.79. A least-squares fit yields a fitted relation of $\log(L_{\rm CO}) = 1 \times \log(L_X) - 33.43$ when considering both Seyfert types of our sample. To rule out the possibility of a correlation driven by the luminosity distance (D^2), we study the correlation between $L_{\rm CO}/L_{\rm FIR}$ and $L_X/L_{\rm FIR}$, and between $L_{\rm CO}/L_X$ and L_X; in both cases we get rid of the distance dependence, if any, and find a significant correlation in both cases.

3. SUMMARY AND DISCUSSION

We have analyzed the gas properties toward the galaxy nuclei of 18 Seyfert 1 and 17 Seyfert 2 galaxies, taken from the *ROSAT*/*IRAS* sample generated by Condon et al. (1998). The CO line is a molecular gas tracer and provides information about the kinematics of the inner galactic disks through the line width. We investigate the CO kinematics and find that the CO line width moderately correlates with the host galaxy inclination for both types of Seyfert galaxies (Figure 2). This may initially suggest that the CO is coplanar with the galactic disk. However, Heckman et al. (1989) showed that the CO emission may also be correlated with the torus. Studies on the relative orientation of a radio jet and the host galactic disk in Seyfert galaxies, e.g., Schmitt et al. (2002) and Nagar & Wilson (1999), have shown that the torus is not coplanar with the galactic disk. The combination of these studies suggests that a small, though not negligible, fraction of the CO emission is coming from the nuclear regions and not solely from the galactic disk. We examine the relation between the CO kinematics and the X-ray power and find a significant correlation between the CO line widths and the hard X-ray luminosities in both AGN types. Based on the assumption of Eddington accretion, we analyze the correlation between the dynamical mass calculated from the CO line width and the BHM calculated from the L_X for Seyfert galaxies. The measured correlation corroborates the recent studies that suggest that the inclination-corrected CO line width is a surrogate for the bulge velocity dispersion of the host galaxies (Shields et al. 2006; Wu 2007), and the BH–bulge relation is obtained with this assumption (Ferrarese & Merritt 2000). As shown in Figure 4, the Eddington limit approximation in our calculations underestimates the $M_{\rm BH}$ by at least a factor of 10 in comparison to the $M_{\rm BH}$–$M_{\rm bulge}$ relation for normal galaxies where $\langle M_{\rm BH}/M_{\rm bulge}\rangle \sim 0.001$ (Marconi & Hunt 2003). In order to get a better understanding of the $M_{\rm BH}$–$W_{\rm CO}$ relation for Seyfert galaxies, we have to rely on more accurate measurements of the $M_{\rm BH}$ and higher resolution images of CO luminosity in future studies.

Yamada (1994) studied the X-ray (0.5–4.5 keV) and CO luminosity relation in a sample of 13 Seyfert 1s and 5 quasars and found a significant correlation. That study suggested a scenario where the star formation activities directly control the mass accretion rate at the central BH, concluding that the more powerful monsters live in the more actively star-forming host galaxies. We analyze the $L_{\rm CO}$–L_X relation with a more extended sample using both Seyfert types and the X-ray bands 0.1–2.4 keV and 0.3–8 keV and find similar correlations between the X-ray and

CO luminosities for both Seyfert types. Two possible scenarios can be considered in the nuclear-activity–total-molecular-gas content relation. First, circumnuclear star formation activity could drive gas into the innermost galactic regions to feed a BH, thus creating a star formation/AGNs connection (Norman & Scoville 1988; Heckman et al. 1989). The CO emission can be related to the infalling interstellar gas feeding the accretion disk of the massive BHs, which is mostly in molecular form located in the central kiloparsecs. Second, the more powerful X-rays from the central BH could provide additional heat to the molecular cloud, enhancing the excitation of CO molecules in the inner region (few parsecs) and enhancing the total CO luminosity. However, the CO emission observed in our sample with CSO typically comes from inner regions of the galaxy disks (2–20 kpc), as determined from the available interferometer data (e.g., Taylor et al. 1999; Israel 2009; Casasola et al. 2008), while most of the X-ray luminosities likely come from the central engine region (a few pc to 100 pc at most). To establish a clear causal connection between molecular gas in the inner 1 kpc and the fueling of nuclear activity will require higher resolution maps of the CO emission. A forthcoming Atacama Large Millimeter Array observation will provide the necessary spatial resolution (Maiolino 2008), which will enable us to obtain much accurate kinematics, extended maps of the distribution, and dynamics of the molecular gas.

The authors thank the CSO staff for their support during observations. We thank the anonymous referees for valuable suggestions that improved the manuscript. We are grateful for interesting discussions with Nick Scoville, Martin Emprechtinger, and Tom Bell. The CSO is founded by the National Science Foundation under the contract AST-08388361. This research has made use of the NASA/IPAC Extragalactic Database (NED), which is operated by the Jet Propulsion Laboratory, California Institute of Technology, under contract with the National Aeronautics and Space Administration.

Facilities: CSO, ROSAT, IRAS, CXO

APPENDIX

CO LINE LUMINOSITY

We have calculated the CO line luminosity using the integrated line intensity ($T\Delta V$), the intensity (I), and the flux ($S_{\rm CO}$). The calculated parameters for each source are listed in Table 2.

To convert from integrated intensity in units of K km s^{-1} into line intensities in units of erg cm^{-2} s^{-1} sr^{-1}, we use the Rayleigh–Jeans relation,

$$I(\mathrm{erg\,cm^{-2}\,s^{-1}\,sr^{-1}}) = \frac{2k_B \times \nu^3}{c^3} \times \frac{T\Delta V\,(\mathrm{K\,km\,s^{-1}})}{B_{\rm eff}} \times 10^6, \quad \text{(A1)}$$

where c is the speed of light, k_b is the Boltzmann constant, $B_{\rm eff}$ is main beam efficiency, and υ is the line frequency in GHz.

Flux in Jy km s^{-1} is derived as follows:

$$S(\mathrm{Jy\,km\,s^{-1}}) = I \times \frac{c}{\nu} \times \Omega_b \times \left(\frac{\nu_0}{\nu}\right)^2 \times 10^{20}, \quad \text{(A2)}$$

where Ω_b is the solid angle in sr. For a Gaussian beam, the solid angle is given by

$$\Omega_b = 1.1333 \times B^2 \times \frac{1}{206265^2}\ \mathrm{sr}, \quad \text{(A3)}$$

where B is the half-power beam width in arcseconds.

We calculate the CO luminosities using the formula in Solomon et al. (1997),

$$L_{\rm CO} = (c^2/2k) \times S_{\rm CO} \times \Delta V \times \nu_{\rm obs}^{-2} \times D_L^2 \times (1+z)^{-3}, \quad \text{(A4)}$$

where D_L is the luminosity distance[7] in Mpc.

REFERENCES

Boller, Th., Meurs, E. J. A., Brinkmann, W., et al. 1992, A&A, 261, 57
Casasola, V., Combes, F., García-Burillo, S., et al. 2008, A&A, 490, 61
Condon, J. J., Yin, Q. F., Thuan, T. X., & Boller, Th. 1998, AJ, 116, 2682
Curran, S. J. 2000, A&A, 144, 271
Edelson, R. A., Malkan, M. A., & Rieke, G. H. 1987, ApJ, 321, 233
Ferrarese, L., & Merritt, D. 2000, ApJ, 529, L9
Gonzalez-Delgado, R. M., & Perez, E. 1993, Ap&SS, 205, 127
Graham, A. W., Erwin, P., Caon, N., & Trujillo, I. 2001, ApJ, 563, L11
Heckman, T. M., Blitz, L., Wilson, A. S., Armus, L., & Miley, G. K. 1989, ApJ, 342, 735
Helou, G., Khan, I. R., Malek, L., & Boehmer, L. 1988, ApJS, 68, 151
Ho, L. C. 2007, ApJ, 669, 821
Isobe, T., Feigelson, E. D., Akritas, M. G., & Babu, G. J. 1990, ApJ, 364, 104
Israel, F. P. 2009, A&A, 493, 525
Kalberla, P. M. W., Burton, W. B., Hartmann, D., et al. 2005, A&A, 440, 775
Kawakatu, N., Saitoh, T. R., & Wada, K. 2005, ApJ, 628, 129
Maiolino, R. 2008, New Astron. Rev., 52, 339
Maiolino, R., Ruiz, M., Rieke, G. H., & Keller, L. D. 1995, ApJ, 446, 561
Maiolino, R., Ruiz, M., Rieke, G. H., & Papadopoulos, P. 1997, ApJ, 485, 552
Marconi, A., & Hunt, L. K. 2003, ApJ, 589, L21
Marconi, A., Risaliti, G., Gilli, R., et al. 2004, MNRAS, 351, 169
Nagar, N. M., & Wilson, A. S. 1999, ApJ, 516, 97
Norman, C., & Scoville, N. 1988, ApJ, 332, 124
Osterbrock, D. E., & Ferland, G. J. 2000, Astrophysics Of Gaseous Nebulae and Active Galactic Nuclei (2nd ed.; GBR: Palgrave Macmillan Limited)
Rickard, L. J., & Harvey, P. M. 1984, AJ, 89, 1520
Rigopoulou, D., Lawrence, A., White, G. J., Rowan-Robinson, M., & Church, S. E. 1996, A&A, 305, 747
Sanders, D. B., Schoville, N. Z., & Soifer, B. T. 1991, ApJ, 370, 158
Schmitt, H. R., Pringle, J. E., Clarke, C. J., & Kinney, A. L. 2002, ApJ, 575, 150
Shields, G. A., Menezes, K. L., Massart, C. A., & Vanden Bout, P. 2006, ApJ, 641, 683
Solomon, P. M., Downes, D., Radford, S. J. E., & Barrett, J. W. 1997, ApJ, 478, 144
Taylor, C. L., Hüttemeister, S., Kein, U., & Greve, A. 1999, A&A, 349, 424
Tully, R. B., & Fisher, J. R. 1977, A&A, 54, 661
Wu, X. B. 2007, ApJ, 657, 177
Yamada, T. 1994, ApJ, 423, L27
Young, J. S., Schloerb, F., Kenney, J. D., & Lord, S. D. 1986, ApJ, 304, 443

[7] For all the sources, we obtained the luminosity distance using the Web site calculator of http://www.astro.ucla.edu/~wright/CosmoCalc.html, using a cosmology of $H_0 = 77\,\mathrm{km\,s^{-1}\,Mpc^{-1}}$, $\Omega_M = 0.27$, and $\Omega_V = 0.73$.